Assessing and mitigating the distortion and stress during electron beam welding of a large shell-flange structure

Yongle Sun [a,b,*], Mike Smith [a], Thomas Dutilleul [c], Steve Jones [c]

[a] Department of Mechanical, Aerospace and Civil Engineering, School of Engineering, The University of Manchester, Sackville Street, Manchester, M13 9PL, UK
[b] Welding Engineering and Laser Processing Centre, School of Aerospace, Transport and Manufacturing, Cranfield University, Cranfield, MK43 0AL, UK
[c] Nuclear AMRC, University of Sheffield, Advanced Manufacturing Park, Rotherham, S60 5WG, UK

ARTICLE INFO

ABSTRACT

Electron beam (EB) welding can efficiently join large-scale components using one single autogenous pass, but it still faces challenges associated with weld-induced distortion and stress. This study investigates EB welding in a low-alloy steel thick-section shell-flange structure for a small modular reactor. A 3D thermal-metallurgical-mechanical model is developed to assess the weld-induced distortion and stress, as well as the strategy to mitigate them. When no restraint is imposed on the circumferential weld plane, an opening and sliding gap develops during the EB welding, which can cause weld defects and even process failure. Restraint through tack welds can effectively mitigate the gapping distortion, but it generates high transient tensile stress in the tack weld. Circumferentially continuous tack weld is preferential over circumferentially discrete tack welds to minimise the tensile stress. The final residual stress is insensitive to the tack-weld restraint, and the stress distribution in the steady-state welding region is broadly similar to that found in plate butt welds. However, concentration of residual stresses with high triaxiality occurs in the weld stop region, with high tensile stresses generated just behind the beam stop location, which cannot be diminished by overlap welding or change of weld stop position. The mechanisms responsible for the distortion and the transient and residual stresses are analysed. This study could provide rational basis for designing weld restraint to control distortion and guiding stress mitigation strategy for crack-susceptible region in EB weldments.

1. Introduction

Electron beam (EB) welding is an efficient process for joining large structural components [1]. Thanks to the high energy density, EB welding can join thick-section components using one single autogenous pass, thereby significantly reducing the welding time and the weld metal volume. EB welding has been applied in many industrial fields [1], and recently there is a growing interest to use EB welding for manufacture of large components in nuclear power plants, such as the reactor pressure vessel and steam generator [2–5]. To safely use this technique in nuclear manufacture, the critical issues of distortion and residual stress must be addressed based on a solid understanding of the mechanisms that control the development of the distortion and stress. Many EB weld mock-ups were produced to gain basic insights into the mechanisms [6–8], while assessment and mitigation of weld distortion and stress in a structure with industrially representative size is scarce.

It is widely recognised that EB welding is a low-distortion process, particularly for large structures. This is because the heat input of EB welding is localised in a narrow region and no filler material is involved. However, a recent study on EB welding in a low-alloy steel plate demonstrated that an opening gap developed ahead of the moving beam when no restraint on the weld plane was imposed during the welding [9]. The gapping distortion is deleterious as it can cause weld defects, beam instability and even process failure [10]. To mitigate the potential gapping distortion, restraint through tack welds on EB weld plane is widely used. However, it is not uncommon that tack welds fail in EB welding practice and then the aforementioned deleterious consequences take place due to the loss of restraint. To evaluate the risk of tack weld failure, the in-process transient stress experienced by the tack weld needs to be determined and assessed, which, however, is difficult if not impossible to measure experimentally. Modelling has proven useful to provide such information and guide the design of tack welds for EB
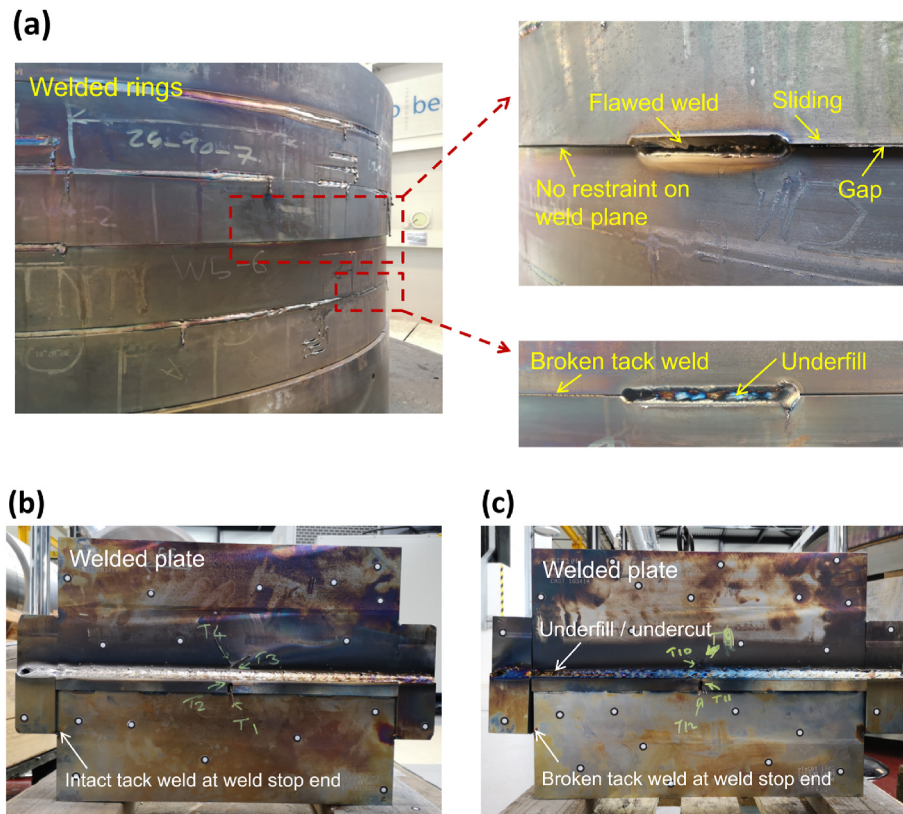
Fig. 1. Weld defects observed in experimental trials of EB welding in steel rings when weld restraint is absent or lost (a). The weld quality for EB welding in steel plates with intact tack weld (b) and broken tack weld (c) is also compared [10].

welding in low-alloy steel plates [9]. However, no modelling study on this issue for circumferential EB weld has been reported in the literature.

There is clear evidence showing that the integrity of tack welds is crucial for the success of EB welding. Fig. 1 shows experimental trials of EB welding in steel rings and plates. For the EB welded rings (Fig. 1a), when restraint was absent on the weld plane, an opening and sliding gap occurred, and consequently the EB weld was flawed; in another scenario, the preinstalled tack welds broke during the EB welding and then underfill defects developed. For the EB welded plates (Fig. 1b and c), the breakage of the tack weld at the EB weld stop end caused underfill and undercut defects. These observations confirmed the importance of weld restraint for circumferential and butt EB welding. To understand the defect phenomena and optimise the tack weld configuration, an EB weld modelling study is needed for providing comprehensive information.

Apart from the gapping distortion and in-process transient stress in tack welds, the final residual stress after EB welding plays an important role in the integrity of the welded structure. Weld residual stress arises from the incompatible deformation caused by the weld-induced thermal cycles, and it is usually detrimental as it can drive, or accelerate, material degradation and cracking [11,12]. For safety-critical structures in nuclear power plants, the industrial code R6 [13–15] considers weld residual stress in structural integrity assessment and provides guidelines to determine the residual stress through modelling. For low-alloy ferritic steels, which are widely used in nuclear components, weld residual stress is complicated due to the effect of solid state phase transformation (SSPT) [12,16]. Consequently, modelling of EB welding in low-alloy steel structures is challenging and it requires consideration of the

coupling between thermal, metallurgical and mechanical response. This requirement poses challenges for modelling of EB welding in large structures, for which the sizes of metallurgical transformed zones, i.e., fusion zone (FZ) and heat affected zone (HAZ), are much smaller than the structural size. Pellereau et al. [17] compared different weld models to predict the residual stresses in a large low-alloy steel component with a curved thick section, and they found that the SSPT is a key factor affecting the residual stress in the EB weldment.

This study is aimed to assess and mitigate the gapping distortion and the transient and residual stresses for EB welding in a large-scale low-alloy steel shell-flange structure for a small modular reactor. A 3D finite element (FE) model is developed to take into account the thermal, metallurgical and mechanical behaviour. Different designs of tack welds on the EB weld plane are evaluated based on their effects on the gapping distortion and the transient and residual stresses. The impact of overlap welding on residual stress is also investigated. In Section 2, the welding and modelling methods are described. The predictions of temperature, microconstituents, hardness, distortion, and transient and residual stresses are presented in Section 3. The results are discussed in Section 4, followed by conclusions in Section 5.

2. Material and method

2.1. EB welding of low-alloy steel shell and flange

Low-alloy steel for nuclear reactor pressure vessels, i.e., SA508 Grade 3 Class 1 steel, was used to manufacture the thick-section shell and

Table 1
Chemical composition (in wt.%) of SA508 Grade 3 Class 1 steel [10].

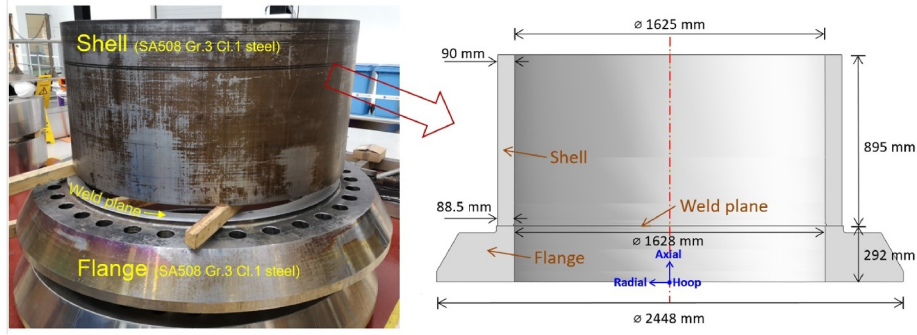| C	Si	Mn	Ni	Cr	Mo	V	Al	Cu	Ti	Fe
0.16	0.25	1.27	0.67	0.17	0.48	0.002	0.017	0.03	0.001	Bal.

Fig. 2. Geometry and configuration of EB welding in the SA508 steel shell and flange (bolt holes in the flange are not considered in the modelling and thus not shown in the sketch).

Table 2
EB welding parameters.

Voltage (kV)	Current (mA)	Speed (mm/s)	Ellipsoidal figure amplitude (mm)	Beam size (mm)
60	450	2	X: 1; Y: 3	1 (Gaussian)

Note: X and Y directions are perpendicular and parallel to the welding direction, respectively.

flange, as well as their joint via EB welding. The chemical composition of the SA508 steel is shown in Table 1. The shell-flange structure is designed for application in a small modular reactor [18]. The dimensions of the shell and flange forgings are shown in Fig. 2. The EB weld plane is at the interface between the two ends of the shell and flange (Fig. 2). The actual flange contains 36 circumferential equidistant holes. Since these holes are far away from the weld, they are ignored in the weld model, so as to facilitate meshing and reduce computational time. The EB welding was performed using the pro-beam® facility located in Nuclear Advanced Manufacturing Research Centre (Nuclear-AMRC), UK, and the welding parameters are summarised in Table 2. The Nuclear-AMRC engineering experience indicates that for EB welding the weld plane gap should be controlled below 1% the component thickness. This means a gap larger than 0.9 mm is unacceptable for the shell-flange structure. The shell and flange were welded in a large vacuum chamber (working volume of 208 m³) and the EB welding process was automated [18,19].

2.2. Thermal-metallurgical-mechanical model

Modelling of EB welding in low-alloy steels, such as SA508 Grade 3 Class 1 steel, is complicated by the SSPT that is caused by the weld-induced thermal cycles. An accurate and reliable model for EB welding must take into account SSPT [12,20]. Herein, a validated semi-empirical SSPT modelling approach [21,22] is adopted, which has been applied in the weld modelling within various R&D programmes, e. g., NeT TG5 [23], NNUMAN [24–26] and MATTEAR [9,10]. The key steps of the sequentially coupled thermal, metallurgical and mechanical modelling of EB welding are briefly described as follows:

a) A volumetric heat source model is used in the EB welding simulation. In principle, the heat source model should be calibrated against thermocouple data and isothermal lines (i.e., boundaries of fusion and heat affected zones that are observed in macrographs). However, these experimental data are not available for this large shell-flange structure. To circumvent this difficulty, the heat source shape parameters are adopted to be similar to a previous EB weld plate mock-up with dimensions of $450 \times 330 \times 80$ [10]. A specialised weld modelling tool, FEAT-WMT [27], is employed for fast thermal analysis to verify the heat source parameters, making sure that the predicted shape and size of the fusion and heat affected zones are reasonable. After definition of the heat source parameters, the time-resolved heat source flux data, which is generated using FEAT-WMT, is imported into the general purpose FE software ABAQUS via subroutines of UEXTERNALDB and DFLUX for thermal analysis therein.

b) The transient temperature field predicted by the ABAQUS thermal model is passed into UVARM subroutine for computation of the kinetics of the SSPT in both the FZ and HAZ, as well as the austenite grain growth in the HAZ. In the FZ, it is assumed that 100% austenite is formed as soon as temperature drops below the melting point, without considering solidification kinetics, and a constant grain size of austenite is assigned. In-process tempering [25] is not considered since the EB welding is a single-pass process. Dilution [26,28] is also irrelevant to the autogenous process of EB welding. The
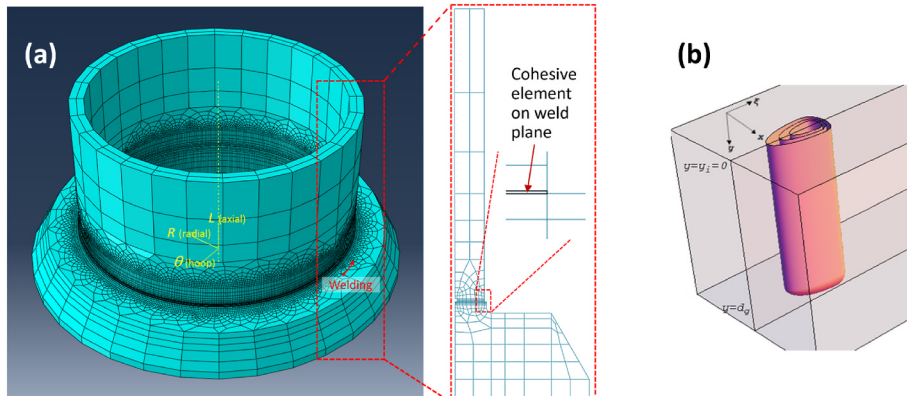

Fig. 3. (a) Geometry and FE mesh of the EB weld model; (b) schematic of the double-ellipsoidal-conical heat source model for EB welding simulation [29].

metallurgical model for austenite formation and decomposition, as implemented in the UVARM subroutine, determines the micro-constituents at every moment during the EB welding.

c) The thermal and metallurgical modelling results are then passed into an ABAQUS mechanical model via subroutines of USDFLD and UEXPAN. The USDFLD subroutine updates material status (i.e., different transformation products) and the corresponding material properties. The UEXPAN subroutine calculates the weld-induced thermal and metallurgical deformation (also including transformation-induced plasticity), which acts as the driving force to generate distortion and stress in the weldment.

A complete temperature-dependent material properties data set for both the SA508 Grade 3 Class 1 steel and its transformation products is available from the previous Net TG5 [23] and NNUMAN [22] research programmes. Theses material properties have been used in the weld modelling within the NNUMAN and MATTEAR projects [10,24–26], and they are also adopted in the welding simulation here, see Appendix. Although no experimental measurements of distortion and stress were attempted for the large shell-flange structure, our previous studies [9, 24] have demonstrated the good accuracy of the EB weld modelling approach employed here.

For completeness, the key aspects and techniques for the EB weld model (Fig. 3a) are described as follows, while the elaboration of the theory and equations can be found in Refs. [21,23–26,28]. The heat source model for the EB welding (Fig. 3b) is based on an idealised volumetric Gaussian distribution of EB power, i.e. double-ellipsoidal-conical (DEC) heat source [29]. It has been demonstrated that the DEC heat source model can well capture EB weld profiles [29]. In this study, two minor heat sources with tiny power were superposed into the main heat source, such that the "dumbbell" profile of the FZ and HAZ observed in the previous EB weld mock-up [10] can be captured. In the simulation the heat source travelled just over the full circumference without overlapping at the weld stop location (i.e., weld start and stop locations are same), unless otherwise stated (Section 2.4). Although a 2D axisymmetric weld model is more computationally efficient, it was not attempted here due to its inaccuracy in capturing the development of 3D distortion and stress, which are the major concerns here. The 3D modelling approach with moving heat source also allows the 3D stress distribution developed at the weld start/stop location to be examined. On the component surfaces, radiation was considered for the whole welding process and the emissivity was taken to be 0.35. The convection was considered only for the cooling after the EB welding (the welded structure was taken out of the vacuum chamber), and the film coefficient was taken to be 1.1×10^{-5} W/(mm^2·K).

For metallurgical analysis, the austenitisation upon heating was modelled using the Leblond-Devaux approach [30], in which an equilibrium fraction of austenite is predefined at different temperatures and an empirical positive time constant is introduced to capture the retardation effect for different heating rates. A two-stage grain growth model [26] was adopted to calculate the austenite grain size in the HAZ. It considered a maximum grain size at temperatures below the grain coarsening temperature while assumed faster unlimited grain growth at higher temperatures. The kinetics of austenite decomposition to ferrite, pearlite and bainite were modelled using a semi-empirical approach originally developed by Kirkaldy and Venugopalan [31] and later refined by Li et al. [21]. This SSPT model requires chemical composition and prior austenite grain size as input and predicts the fractions of ferritic phases formed during cooling. For martensite transformation, the classic Koistinen-Marburger model [32] was employed. Furthermore, a rule-of-mixture was used to calculate the hardness based on the predicted fractions of different microconstituents. More details about the metallurgical modelling approach can be found in Refs. [21,23–26, 28].

For mechanical analysis, cohesive elements were used to capture the restraint condition on the weld plane, i.e., an additional thin layer (0.1

mm thick) of cohesive elements only possessing elastic properties was added on the weld plane (Fig. 3a), of which the two end surfaces were bonded to the two opposing ends of the shell and flange, respectively. Tack weld locations were specified in the thin layer, and the FE nodes within each tack weld were restrained from separation via assuming extremely high stiffness of the cohesive elements. For the unrestrained FE nodes, they can separate from the weld plane, but are not allowed to penetrate. Such a condition was implemented through assuming extremely low stiffness for separation but extremely high stiffness for penetration. To simulate the progressive establishment of central restraint due to the EB welding itself, restraint was imposed when the heat source passed the cohesive elements, as implemented through updating the field variable that controls the cohesive element stiffness. It should be mentioned that the rise in the stiffness of cohesive elements occurred at high temperature when the heat source just passed the elements, meaning that the deformation of those cohesive elements, which underwent separation before the heat source passed, was drastically reduced afterwards. Nevertheless, such a change of the deformation can be accommodated by the plastic deformation of the weld material, which is very soft at the high temperature. This technique has been applied to EB weld modelling for a SA508 Grade 4 N steel plate [9].

Regarding the boundary conditions in the mechanical model, three neighbouring nodes on the bottom of the flange were restrained to solely prevent rigid body motion of the shell-flange structure. These nodes were 180° away from the weld start position. Normally, the boundary condition to solely eliminate rigid body motion is not unique, and the adopted boundary condition renders the 180° position as the reference for quantifying the displacement field. Gravity was not considered in the model and hence the predicted distortion and stress were solely driven by the EB welding process.

It was necessary to make assumptions about the weld start and stop transient conditions. The weld was modelled with an instantaneous start and stop (i.e., no ramp-up or ramp-down of the beam power), and with no attempt to "slope in" or "slope out" the weld pool profile. This approach is likely to lead to an overestimate of the stress concentration at the weld stop end, but it is the only feasible one in the absence of an understanding of the complex interaction between the beam parameters and the process of keyhole formation and collapse. Abrupt start/stop techniques are also used in engineering practice, so the results of this analysis are potentially applicable to a real-world approach.

One challenge facing the present modelling analysis is the significant computational burden due to the sharp mismatch between the size (~15 mm) of FZ/HAZ and the size (~2000 mm) of the shell and flange. In addition, the time increment must be sufficiently small to ensure the accuracy in capturing the SSPT kinetics coupled with the transient temperature field. The FE mesh has been optimised to capture the high gradients of physical variables across the FZ and HAZ, whilst minimising the total number of elements (Fig. 3a). Meanwhile, linear elements had to be used to reduce the computational time to an acceptable level, given the large size of the structure (also results in long welding time). The thermal model comprises 125,888 linear heat transfer brick elements (Abaqus designation DC3D8), while the mechanical model consists of 125,888 elements, including 121,552 eight-node linear brick, reduced integration elements (ABAQUS designation C3D8R) and 4336 eight-node cohesive elements (ABAQUS designation COH3D8). The co-ordinates of all these elements between thermal and mechanical models are identical (Fig. 3a). It should be noted that the COH3D8 elements were replaced with C3D8R elements when the weld plane was fully restrained in the mechanical model.

Although best effort was made for trade-off between prediction accuracy and computational efficiency, the computational time was still very long mainly due to the large size of the shell-flange structure and the complexity of the multiphysics problem handled. Typically, for each analysis case, the entire thermal-metallurgical-mechanical simulation took 44 days using 72 Intel Haswell CPUs.
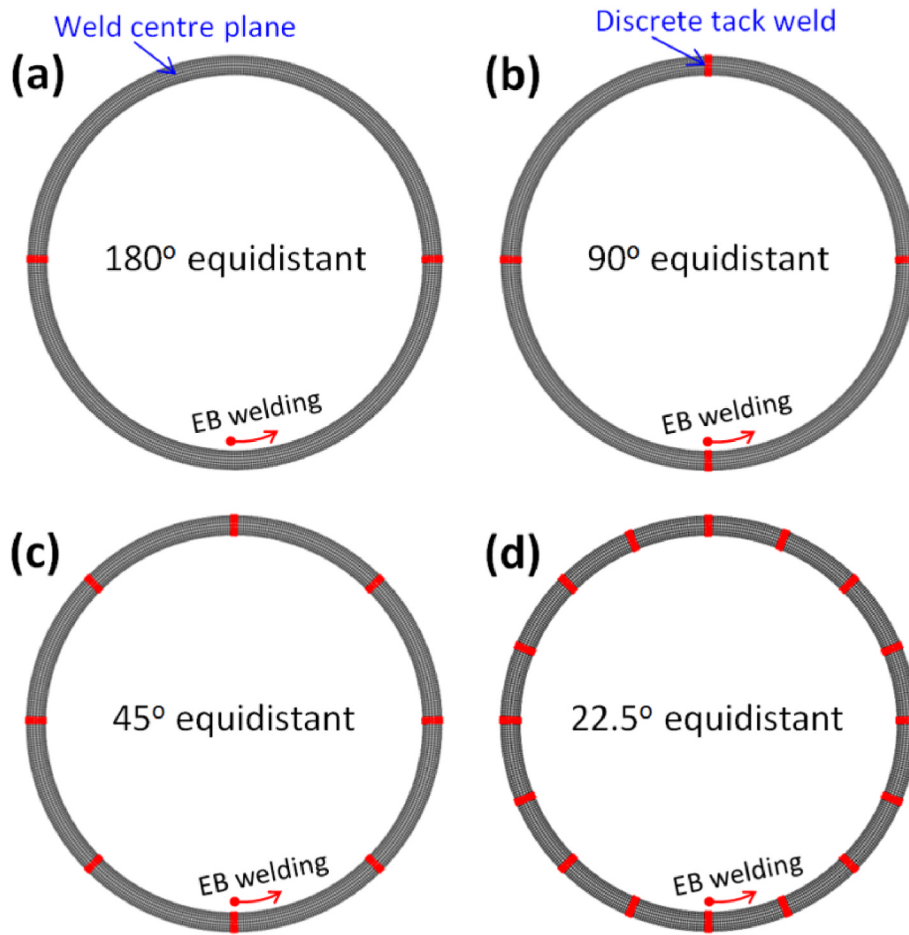
Fig. 4. Design of circumferentially equidistant discrete tack welds at angular intervals of 180° (a), 90° (b), 45° (c) and 22.5° (d) on the EB weld plane. Each tack weld is 20 mm wide in the circumferential direction.
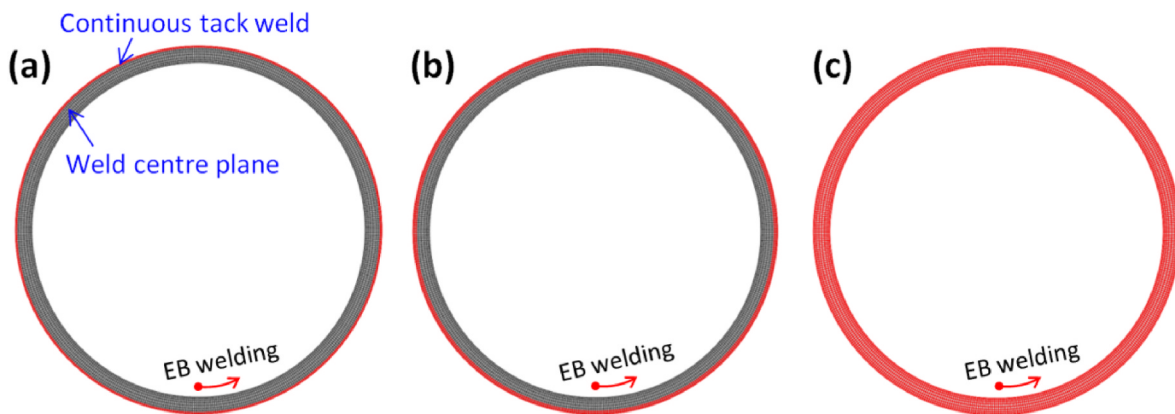

Fig. 5. Design of circumferentially continuous tack welds penetrating from the outer surface of the structure with depth of 7 mm (a), 16 mm (b) and full wall thickness, i.e., full restraint (c).

2.3. Design of tack-weld restraint

Figs. 4 and 5 show the circumferentially arranged discrete and continuous tack welds on the EB weld plane, respectively. The discrete through-thickness tack welds (20 mm wide in circumferential direction) were equidistantly located on the EB weld plane, and the angular distance between each tack weld was taken to be 180°, 90°, 45° and 22.5° in the four analysis cases (Fig. 4). The continuous tack weld covered the full circumference, and the penetration depth from the outer surface of

the structure was taken to be 7 mm, 16 mm and full wall thickness in the three analysis cases (Fig. 5).

In the actual manufacturing, the same EB welding machine was used to produce the tack welds with adoption of low heat input, for which the EB current and voltage were 100 mA and 60 kV, respectively, following circular figure with an amplitude of 1.3 mm, and the welding speed was 10 mm/s. It should be noted that the process for implementing the tack welds was not modelled; this simplification should not affect the final results, since the EB welding will re-melt all the tack welds which are
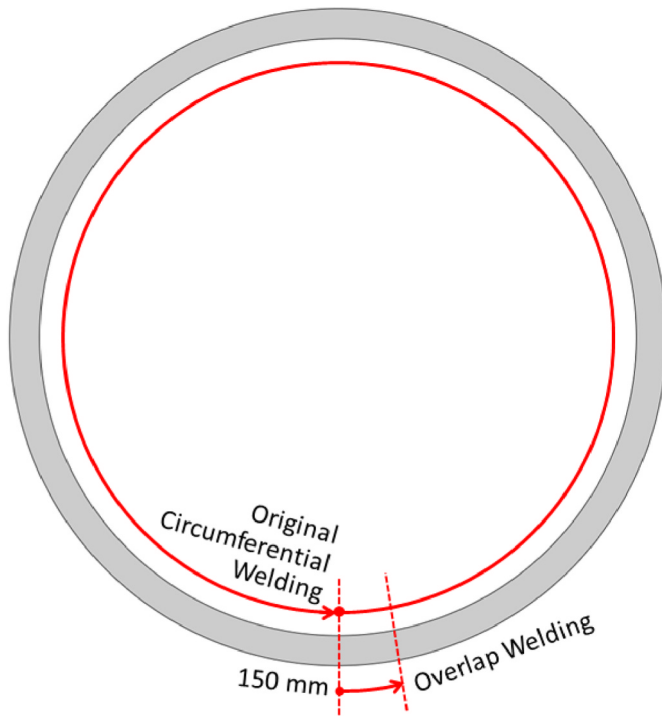
Fig. 6. Illustration of the overlap EB welding that travels over 150 mm from the stop position of the original circumferential EB weld on the weld plane.

used mainly for restraint purpose.

2.4. Weld overlap

Overlap EB welding in the shell-flange structure was modelled by restarting the EB weld model developed in Section 2.2, in which the EB welding was assumed to just cover the circumference of the structure [10]. Fig. 6 illustrates the original and overlap EB welding paths on the weld plane. The restart of the weld model includes two steps: first, determining the new transient temperature field using the thermal

solution obtained in Section 2.2 as the initial condition, with the identical heat source travelling over the overlap distance; second, based on the new thermal solution, determining the new metallurgical and mechanical response using the variables obtained in Section 2.2 as the initial condition.

3. Results

3.1. Thermal and metallurgical predictions

Fig. 7 shows the temperature distributions on both circumferential and axial sections, as well as the temperature histories at notional thermocouple locations on both outer and inner surfaces. Fig. 7a shows the temperature distribution on the weld plane when the half structure was welded. Fig. 7b shows the peak temperature distribution on an axial section 180° away from the weld start position, representative of steady-state welding condition. The FZ and HAZ are distinguished based on the peak temperature ranges, i.e., $T_{max} \geq 1480$ °C for FZ and 760 °C $\leq T_{max}$ < 1480 °C for HAZ (Fig. 7b). Typical transient temperature profiles at four nodes are also shown in Fig. 7c.

The predicted cooling rate at 700 °C falls in the range of 5–30 °C/s, while most regions in the FZ and HAZ were cooled at ~10 °C/s (Fig. 8a). Such a cooling rate is anticipated to produce bainite for SA508 Grade 3 Class 1 steel [22]. Indeed, the weld model predicted that bainite is dominant in the FZ and HAZ (Fig. 8b), although some martensite was also formed. Fig. 8c shows the contour map of predicted hardness distribution and Fig. 8d shows the predicted cross-weld line profiles of hardness. The hardness in the weld centre is slightly lower than the hardness in the HAZ.

3.2. Distortion

Fig. 9 shows the displacement magnitude of the shell and flange during the EB welding without any applied restraint on the weld plane. It is evident that an opening and sliding gap was generated between the shell and flange. Given the large size of the structure, gravity may help to reduce the gapping distortion to some extent, depending on how the shell and flange are positioned during the welding in the real world. However, it is unlikely to eliminate the gap solely by gravity, since the gapping is manifested as 3D distortion (Fig. 9), while the gravity acts
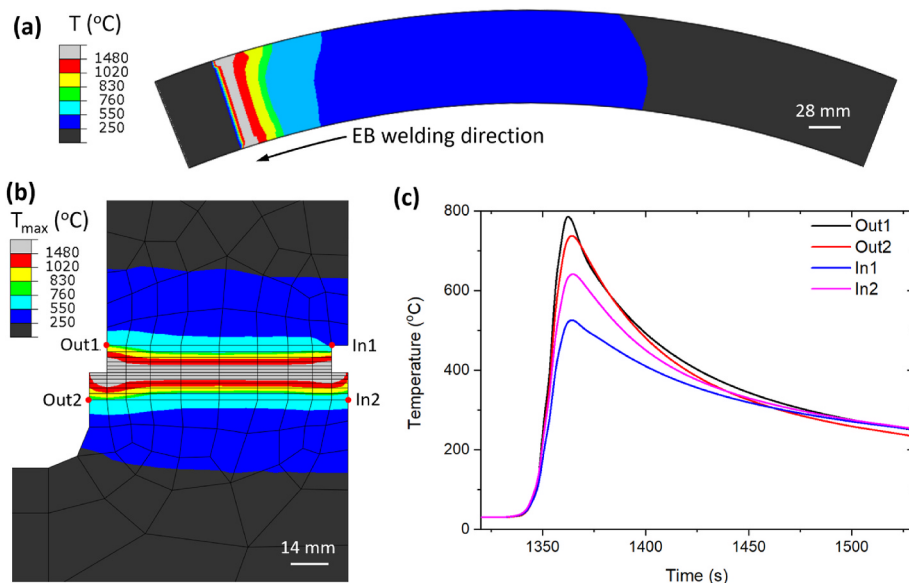

Fig. 7. (a) Transient temperature field on the circumferential EB weld plane after welding half structure; (b) peak temperature distribution on an axial section with an angular distance of 180° from the EB weld start position; (c) temperature histories on the outer surface points (i.e., Out1 and Out2) and inner surface points (i.e., In1 and In2), as indicated in (b).
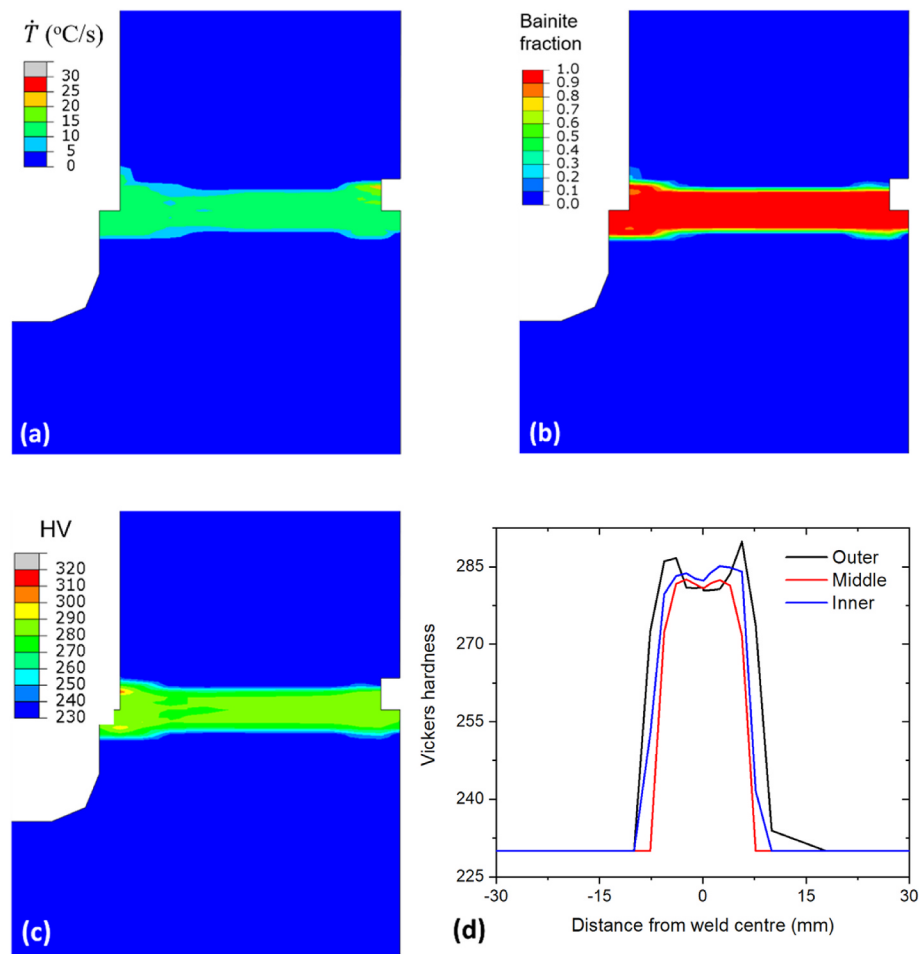
Fig. 8. Contour maps of predicted variables on the axial section (steady-state welding region) with an angular distance of 180° from the EB weld start position: (a) cooling rate at 700 °C (note: cooling rate is set to be zero when peak temperature is lower than 700 °C); (b) fraction of formed bainite; (c) hardness distribution. The cross-weld line profiles of hardness distributions along outer, middle and inner paths are shown in (d).
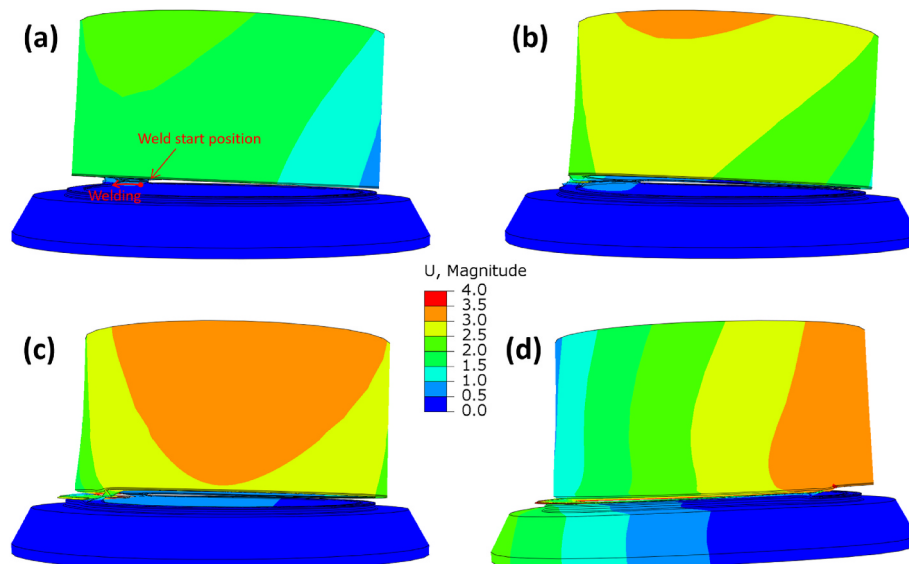

Fig. 9. Geometric configuration and displacement magnitude (unit: mm) of the shell-flange structure when the unrestrained EB welding passed over 1/20 (a), 1/8 (b), 1/4 (c) and 1/2 (d) circumference. Note that the deformation is scaled by a factor of 50 to aid visualisation.
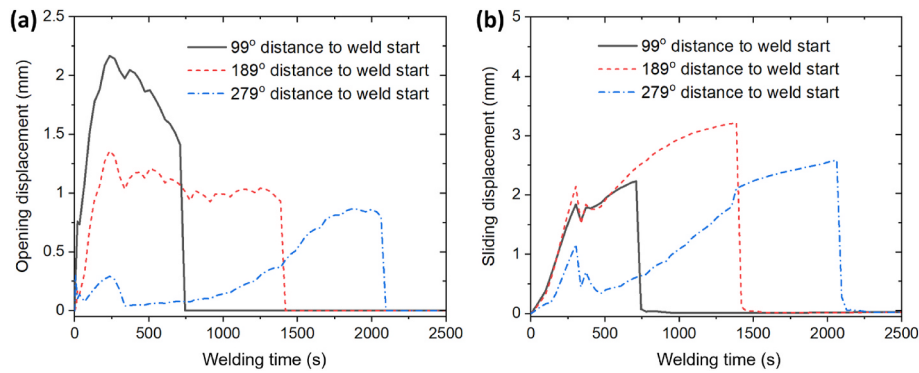
Fig. 10. Evolution of the opening (a) and sliding (b) displacements for mid-thickness locations on the weld plane with different angular distances to the EB weld start position.
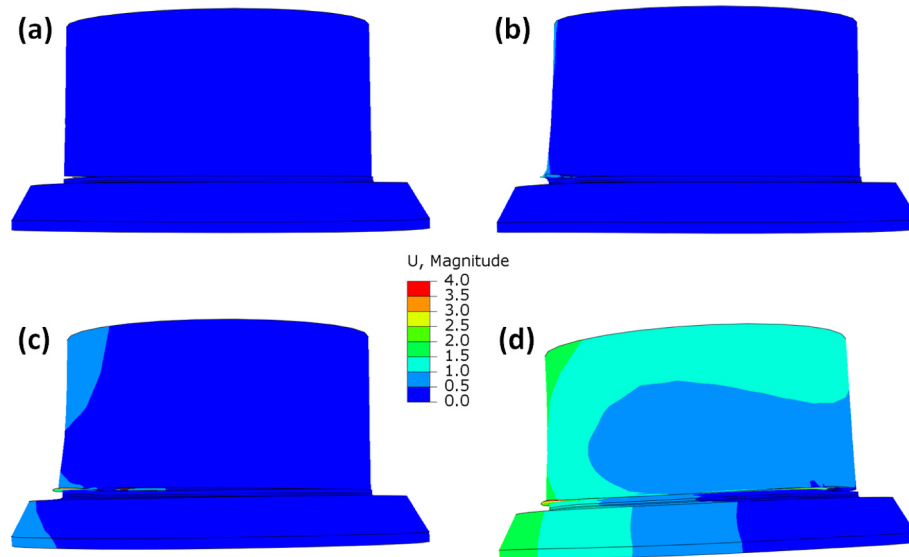

Fig. 11. Geometric configuration and displacement magnitude (unit: mm) of the shell-flange structure when the restrained EB welding passed over 1/20 (a), 1/8 (b), 1/4 (c) and 1/2 (d) circumference. Discrete tack welds with 90° intervals (Fig. 4b) were chosen as an illustration case. Note that the deformation is scaled by a factor of 50 to aid visualisation.

Table 3
Maximum opening and sliding displacements for mid-thickness locations on the weld plane with different angular distances to the EB weld start position.

Unit: mm	99° distance to weld start		189° distance to weld start		279° distance to weld start	
	Opening	Sliding	Opening	Sliding	Opening	Sliding
No restraint	2.17	2.23	1.36	3.22	0.86	2.58
180° tacks	0.54	0.21	1.09	0.43	0.49	0.25
90° tacks	0.50	0.25	0.50	0.47	0.49	0.38
45° tacks	0.39	0.42	0.40	0.63	0.39	0.70
22.5° tacks	0.25	0.30	0.27	0.33	0.25	0.31
7 mm deep tack	0.16	0.08	0.17	0.08	0.15	0.07
16 mm deep tack	0.08	0.16	0.08	0.22	0.08	0.19

only in one direction.

Fig. 10 is focused on the opening and sliding displacements for different mid-thickness locations on the weld plane. The locations for inspection were selected to avoid coincidence with the tack-weld locations. The gapping distortion increased with the welding proceeding, and the closer to the weld start position, the earlier the increase. No further gapping occurred after the heat source passed the inspected

locations, for which the maximum opening and sliding displacements were 2.2 mm and 3.2 mm, respectively.

Fig. 11 shows the displacement magnitude during EB welding with the restraint for which 90° equidistant tack welds were considered in the model (Fig. 4b). It is clearly seen that the tack-weld restraint effectively mitigated the gapping distortion around the weld plane. Table 3 summarises the maximum gapping distortions for different locations under various restraint conditions. The full restraint condition was not included since it eliminated the opening and sliding gap. It is evident that the introduction of the tack welds significantly reduced the gapping distortion, and in general the more extensive the tack welds, the lower the gapping distortion. It is also interesting to see that the sliding displacement exhibits complicated dependence on the restraint condition, which is associated with unique weld deformation in through-thickness direction, as examined below.

Fig. 12 shows the distribution of displacement magnitude in the axial section of the final welded structure. The unrestrained EB welding led to an underfill defect in the final weld (Fig. 12a), mainly due to the opening and sliding gap between the shell and flange (Figs. 9 and 10), which cannot be filled since the EB welding does not involve filler, and such a defect was avoided when tack-weld restraint was applied (Fig. 12b). The final weld configuration is similar between the tack-weld restraint (Fig. 12b) and full restraint (Fig. 12c), i.e., the weld plane expanded
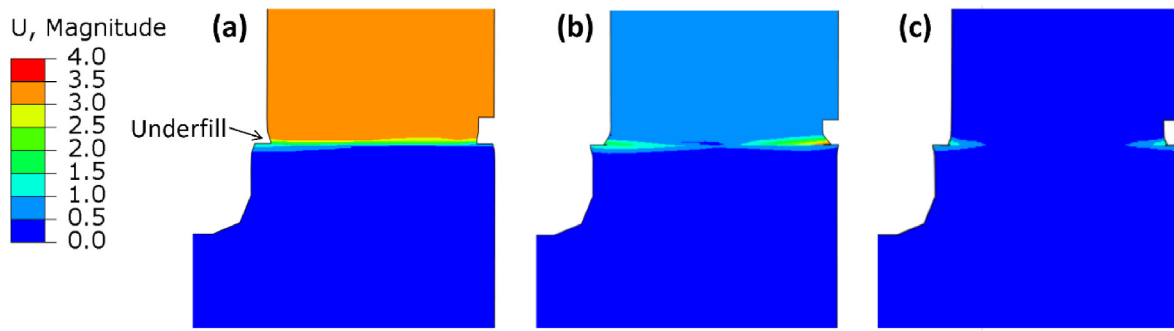
Fig. 12. Final geometric configuration and displacement magnitude (unit: mm) as shown on the axial section (steady-state welding region) with an angular distance of 180° from the EB weld start position: (a) unrestrained EB welding; (b) 90° tack-weld restrained EB welding; (c) fully restrained EB welding.
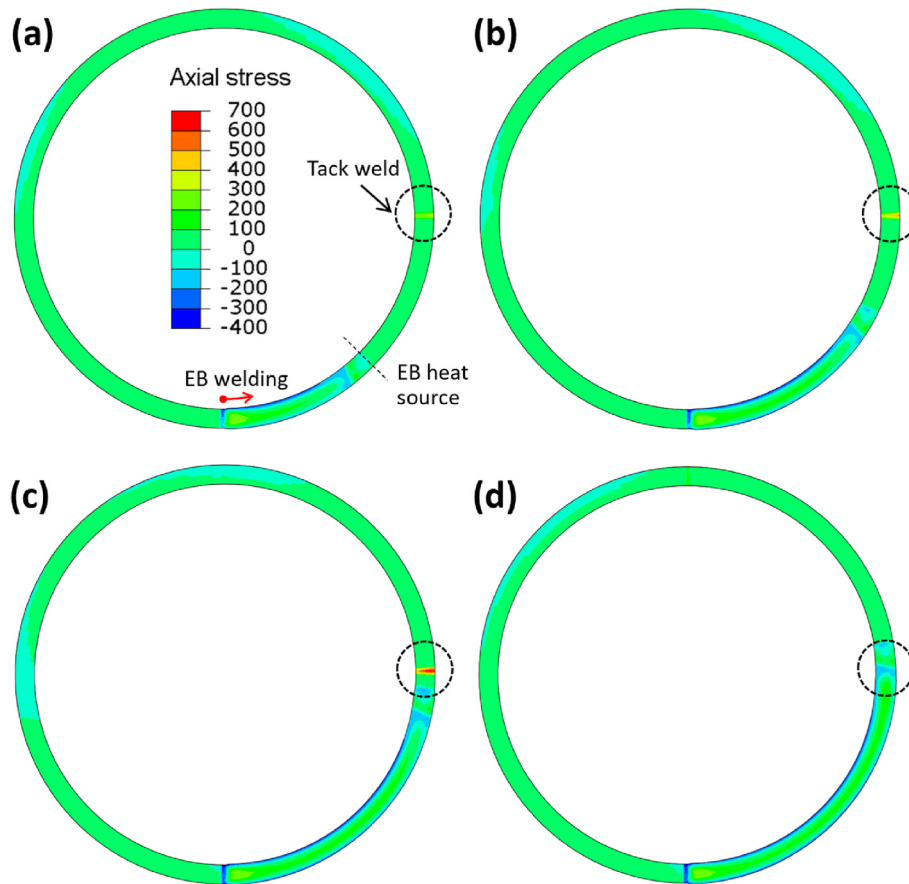

Fig. 13. Axial stress (unit: MPa) distributions on the EB weld plane with 90° equidistant tack welds: (a) welded over 45°; (b) welded over 63°; (c) welded over 85.5°; (d) welded over 99°.

through the wall thickness. This is because there was little constraint for the through-thickness thermal expansion on the weld plane during heating, and the expansion produced a weld metal thicker than the component in absence of gapping distortion, thanks to the restraint on the weld plane.

3.3. Transient stress

Fig. 13 shows the evolution of the axial stress on the weld plane during the EB welding with 90° equidistant tack welds. High tensile stress up to 690 MPa developed when the heat source approached the tack weld that is 90° away from the weld start position, but the restraint-induced high tensile stress disappeared after the heat source passed the tack weld.

Fig. 14 shows the axial stresses at the tack welds that are 180° and 270° away from the EB weld start position, as obtained by the model incorporating 90° equidistant tack welds. High tensile stresses, of magnitude similar to that for the tack weld shown in Fig. 13, were generated, which also dropped to a low level after the heat source passed the tack weld. In other words, the sequence of the tack welds encountering the heat source hardly affected the magnitude of restraint-induced stresses.

Fig. 15 shows the axial stress distributions on the weld plane in different stages of the EB welding with a 7 mm deep continuous tack weld. High tensile stress up to 490 MPa was generated within the tack weld immediately ahead of the EB weld; the magnitude of the peak tensile stress is substantially lower than that for the 90° equidistant discrete tack welds (Figs. 13 and 14). Unlike the alternate rise and drop
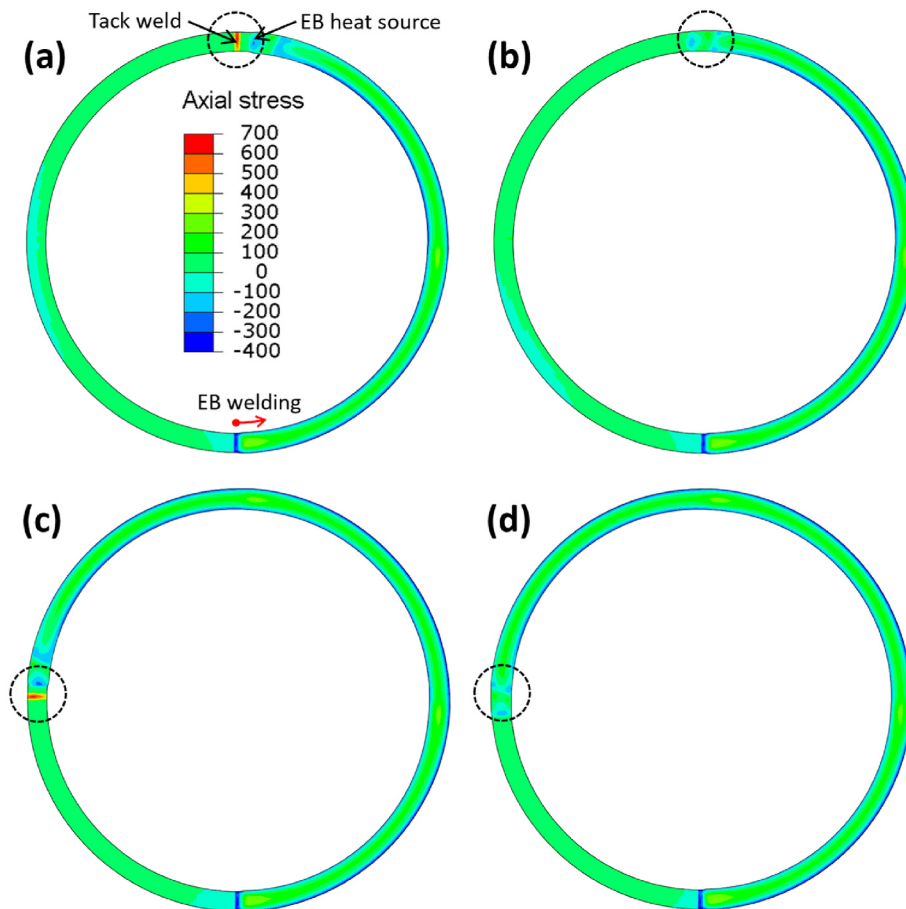
Fig. 14. Axial stress (unit: MPa) distributions on the EB weld plane with 90° equidistant tack welds: (a) welded over 175.5°; (b) welded over 184.5°; (c) welded over 265.5°; (d) welded over 274.5°.

of tensile stress induced by discrete tack welds (Figs. 13 and 14), the continuous tack weld led to an almost constant local stress field around the EB weld front.

Fig. 16 compares the axial stress evolution during the EB welding for discrete tack welds with different angular intervals. It is interesting to see that the peak tensile stress at the tack weld was almost unchanged when the angular interval between each tack weld reduced from 180° to 22.5°. Another interesting feature is that the tensile stress at the tack weld increased rapidly, when the heat source approached the tack weld from 31.5° away to 4.5° away. Therefore, it appears that an angular distance of 4.5° between the heat source and tack weld is critical for high tensile stress development.

Fig. 17 compares the axial stresses around the EB weld front in different stages of the EB welding for continuous tack welds with different depths from the outer surface. Increasing the tack weld depth from 7 mm to 16 mm led to a reduction of peak tensile stress from 490 MPa to 420 MPa and a shorter span of the tension region ahead of the EB weld. Apart from this difference, the stress distribution is similar.

3.4. Residual stress

For residual stress analysis, we first consider the "steady-state" stresses remote from the weld start/stop location. These are not necessarily the most severe stresses developed within the welded structure. It should be mentioned that the initial yield strengths at room temperature are 402 MPa and 420 MPa for the base material and formed bainite (dominant in FZ and HAZ, Fig. 8), respectively. Fig. 18 shows the von Mises stress distribution in the welded shell-flange structure. It is interesting to see that the peak stress is located outside the weld centre.

Such a feature of residual stress distribution is typical for steels experiencing SSPT during welding [24].

Figs. 19–21 show the distributions of the radial, hoop and axial residual stresses, respectively, on the axial section corresponding to steady-state welding for different restraint conditions. Overall, the residual stress distributions are similar between different restraint conditions. Across the mid-thickness path, from the weld centre to the axial end, the radial stress firstly increases from a value close to zero, reaching a peak tensile stress of ~200 MPa close to the outer boundary of the HAZ, and then decreases and becomes compressive in the base material. The hoop stress is of highest magnitude compared to the radial and axial stresses, due to the largest constraint in circumferential direction. The hoop stress is tensile at the weld centre; for locations further away from the weld centre, the hoop stress increases to a peak value and then drops until becoming compressive. Figs. 19 and 20 imply that the line profiles of the radial and hoop stresses across the EB weld exhibit a "M"-shape distribution typical for low-alloy steel weld [12,16]. The distribution of axial stress is distinctive (Fig. 21). An axial tension region, with a peak stress up to 200 MPa, was found in the centre and near the inner surface, while an axial compression zone was present near the outer surface. Such an axial stress distribution feature is also seen in single-pass pipe welds, which can be attributed to the weld shrinkage in hoop direction resulting in the tendence for the materials near the outer surface and inner surface to move towards and away from the weld plane, respectively.

In the second part of the residual stress analysis, the development of stress concentration at the weld stop position (coincident with the weld start position for non-overlapping EB welding) was analysed. As shown in Fig. 22, large axial stresses developed at the weld stop position due to
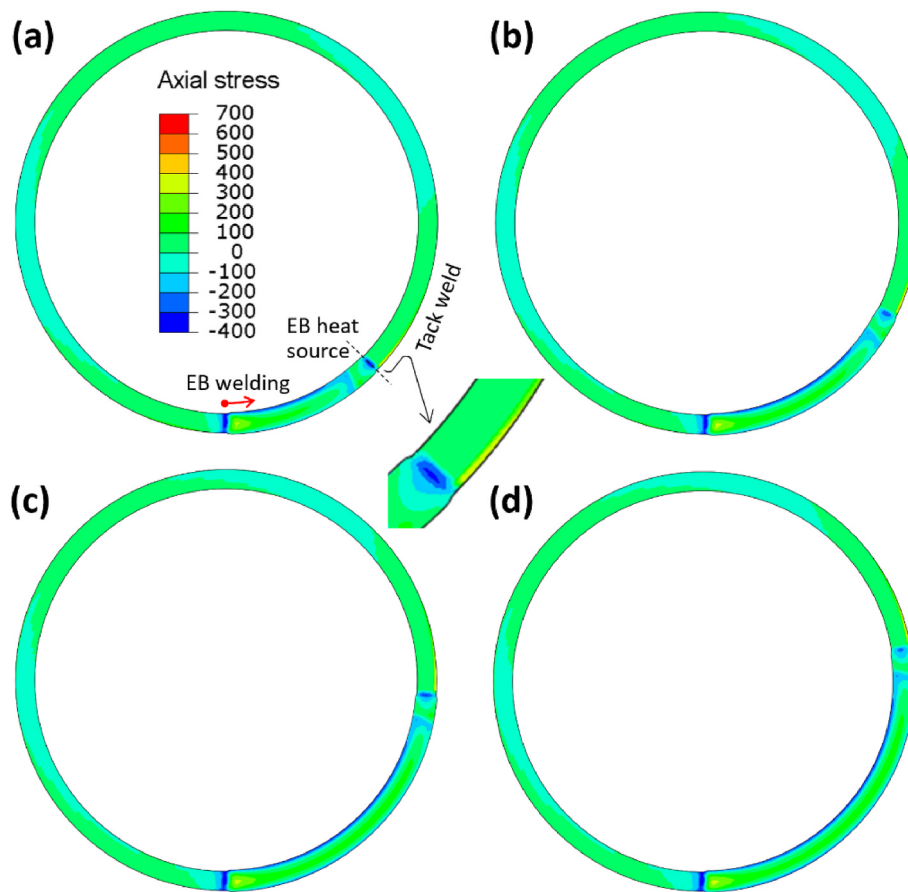
Fig. 15. Axial stress (unit: MPa) distributions on the EB weld plane with 7 mm deep continuous tack weld: (a) welded over 45°; (b) welded over 63°; (c) welded over 85.5°; (d) welded over 99°.

three-dimensional constraint around the weld pool there, with peak tensile stresses in the trailing region where solidification occurs last, balanced by compressive stresses ahead of the final weld pool location. The different restraints on the weld plane barely affect the stress distributions.

In the third part of the residual stress analysis, we examined the effect of overlap welding on the stress concentration near the final weld stop position. Only the modelling results for full restraint on the weld plane are presented (Fig. 23), since the residual stress is insensitive to the restraint design (Figs. 19–22). Similar to the modelling results for the EB weld without overlapping (Fig. 22), high tensile axial stress was generated immediately behind the overlap EB weld stop position, which was balanced by the compressive stress developed immediately ahead of the weld stop position (Fig. 23a). At the stress concentration location, the distribution profiles of the hoop and radial stresses (Fig. 23c and d) on the axial section are typical for weld residual stresses that are affected by SSPT, i.e., the level of tensile stress is lowered in the weld centreline while peak tensile stress is shifted towards the base material. The axial stress distribution (Fig. 23b) on the axial section is distinctive, with no drop of tensile stress found in the weld centreline. The peak tensile axial stress that developed just behind the stop position reaches 500 MPa (in excess of the yield strength, see Table A2 in Appendix), compared with a general peak level of less than 200 MPa (Fig. 21). The peak hoop stress reaches 800 MPa, compared with approximately 600 MPa in the steady-state condition (Fig. 20), while the peak radial stress reaches 500 MPa, compared with less than 250 MPa in the steady-state condition (Fig. 19). These extremely high stresses reflect the strongly triaxial conditions generated at the stop position, and the overlap EB welding did not diminish the stress concentration there, where the welding was stopped abruptly.

4. Discussion

Low distortion is one primary advantage of EB welding, which is particularly beneficial and often crucial for the joining of large components [1]. However, EB welding can still generate large distortion if no restraint is imposed during the welding. The present weld modelling results demonstrated that an opening gap over 2 mm and a sliding gap over 3 mm were generated in the shell-flange structure (Figs. 9 and 10) without any restraint on the weld plane. For EB welding in plates [9], only opening gap developed. The gapping distortion can be attributed to the thermal expansion in an extensive region heated by the rapidly travelling EB heat source (Fig. 7a). Although the gravity could somehow help to hinder the gap development, the significant nonuniform distortion is unlikely to be eliminated solely by the gravity of the component without proper restraint.

The gapping distortion caused position mismatch between the shell and flange during the welding (Fig. 9) and an underfill defect in the final weld (Fig. 12). Indeed, these defects were also observed in experimental EB weld trials (Fig. 1). The underfill occurred because the EB welding is an autogenous process and there is no filler material to fill the gap between the shell and flange. In practice, the gap ahead of the beam could also cause beam instability and even process failure. For a focused beam, a gap above 0.1 mm normally cannot be tolerated [1]. For a defocused or oscillated beam, the gap tolerance could be relaxed (e.g., 1% component thickness), but the gap still poses a threat to the stability of the beam and can disturb the keyhole formed in the autogenous welding process. Therefore, gapping distortion is always detrimental.

Tack welds prove effective to mitigate, or even eliminate, the gapping distortion. However, the tack welds are susceptible to large tensile stress during the EB welding, and thus an optimal design is needed to
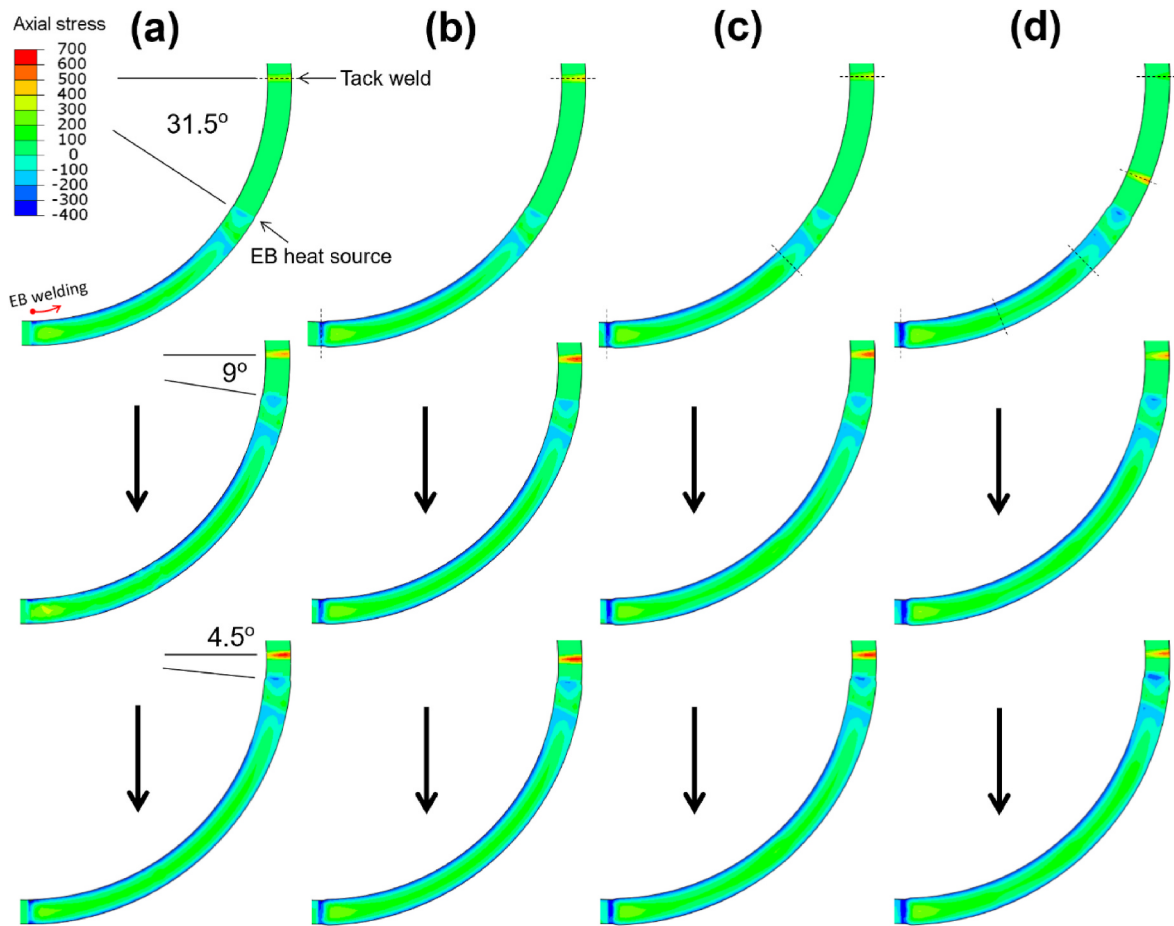
Fig. 16. Comparison between axial stress (unit: MPa) distributions on the EB weld plane with 180° (a), 90° (b), 45° (c) and 22.5° (d) equidistant tack welds. Dashed lines indicate the positions of tack welds. Angular distance from the heat source to the tack weld ahead, i.e., 31.5°, 9° and 4.5°, is also shown.
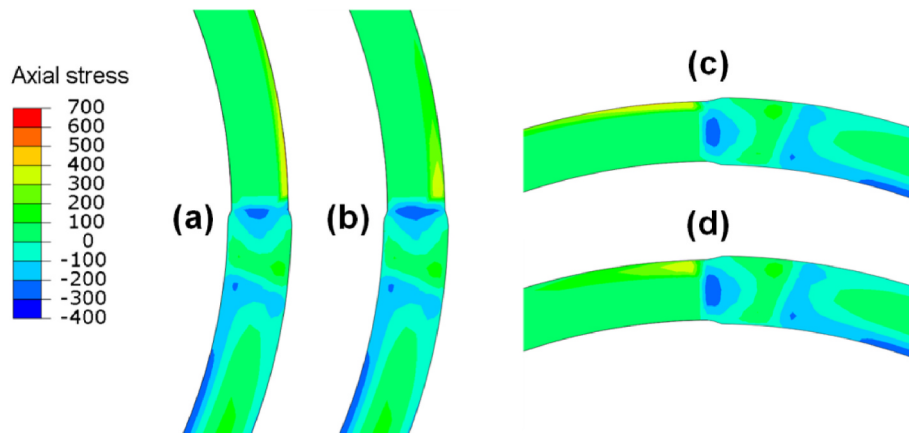

Fig. 17. Comparison between axial stress (unit: MPa) distributions on the EB weld plane with 7 mm (a, c) and 16 mm (b, d) deep continuous tack welds, when the shell-flange structure was welded over 90° (a, b) and 180° (c, d).

minimise the risk of breaking tack welds and the resultant loss of restraint. The design of tack-weld restraint for EB welding is usually based on engineering experience or experimental trial-and-error, rendering the practice as a "black-art", which may face challenges in different engineering scenarios. The present study provides insights into the tack weld effects and lays a rational basis for the optimisation of tack welds.

High tensile stress up to 690 MPa developed at the 20 mm wide discrete tack welds when the heat source approached within a critical angular distance of 4.5°, and surprisingly the peak tensile stress was

insensitive to the number of the tack welds imposed (Fig. 16). To examine the effect of the tack weld width, an additional analysis was carried out. Fig. 24 shows the evolution of axial stress when the heat source approached the 90° equidistant tack welds with a circumferential width of 100 mm. In such a case, peak tensile stress up to 550 MPa developed at the tack weld. This indicates that the increase in tack weld width can effectively reduce the peak tensile stress experienced by the tack weld. Indeed, when the continuous circumferential tack weld was used, the peak tensile stress further reduced to 490 MPa for 7 mm depth
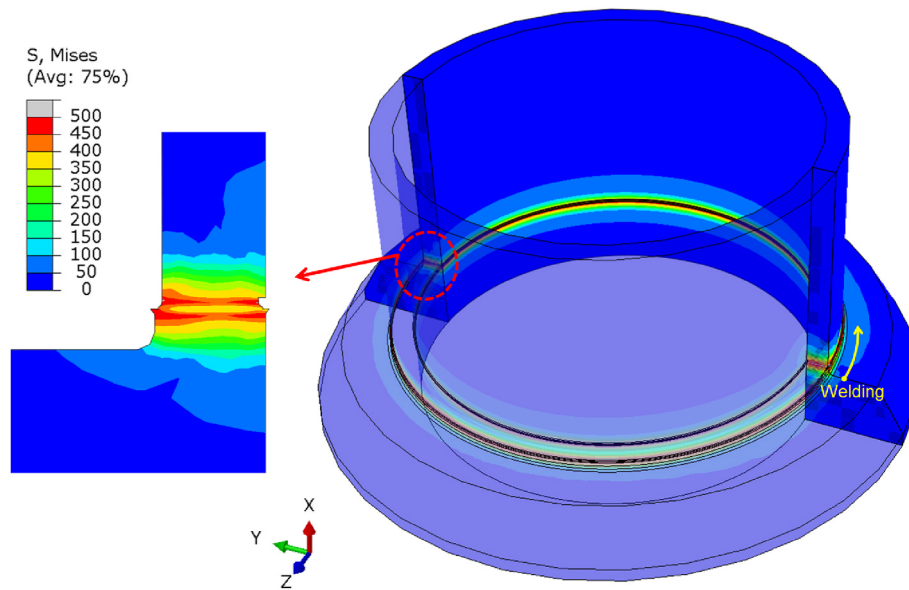
Fig. 18. 3D distribution of Mises equivalent stress (unit: MPa) obtained from fully restrained EB weld model (Fig. 5c). Note that half the model is set translucent and the stress contour on an axial section corresponding to half weld length is also shown.
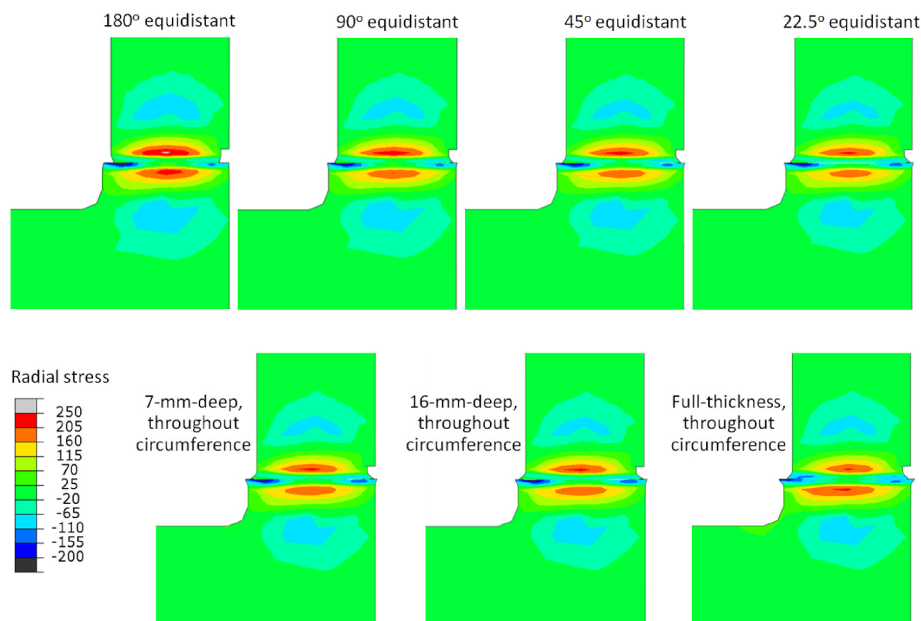

Fig. 19. Radial residual stress (unit: MPa) distributions on the axial section (steady-state welding region) with an angular distance of 180° from the EB weld start position for different restraint conditions.

and 420 MPa for 16 mm depth. Such stress reduction can be attributed to the increase in effective area to withstand the reaction force associated with the weld restraint. Therefore, circumferentially continuous tack weld is preferential to mitigate the risk of loss of restraint due to the potential tack-weld breakage caused by high tensile stress.

After the EB welding, bainite is dominant in the FZ and HAZ of the welded SA508 Grade 3 steel shell-flange structure. The metallurgical predictions are similar to those for EB weld plates [10,24]. The bainite transformation introduced metallurgical expansion deformation during cooling and thereby reduced the tensile residual stress in the EB weld, but it did not lead to compressive residual stress in the FZ and HAZ, in contrast to SA508 Grade 4 N steel weld plates [9,10], for which the FZ and HAZ are dominated by martensite and subjected to pronounced compressive stress. This difference arises because the bainite

transformation occurs at higher temperature than the martensite transformation, and hence it is less effective to generate compressive stress [33].

The residual stresses in the steady-state region of the welded shell-flange structure are broadly similar in magnitude to plate butt welds [10,24], and the FE predictions are consistent with previous measurements of residual stresses in an EB welded A508 low-alloy steel component with curved thick section [34]. The distributions of hoop and radial residual stresses exhibit a similar feature that the tensile stress in the weld centre is suppressed and the peak tensile stress is shifted towards the base material, and such a feature is typical for weld residual stresses affected by SSPT in ferritic steels [12,23,33,35].

Most notably, a very large stress concentration is predicted just behind the weld stop location. The stresses generated in the

Fig. 20. Hoop residual stress (unit: MPa) distributions on the axial section (steady-state welding region) with an angular distance of 180° from the EB weld start position for different restraint conditions.
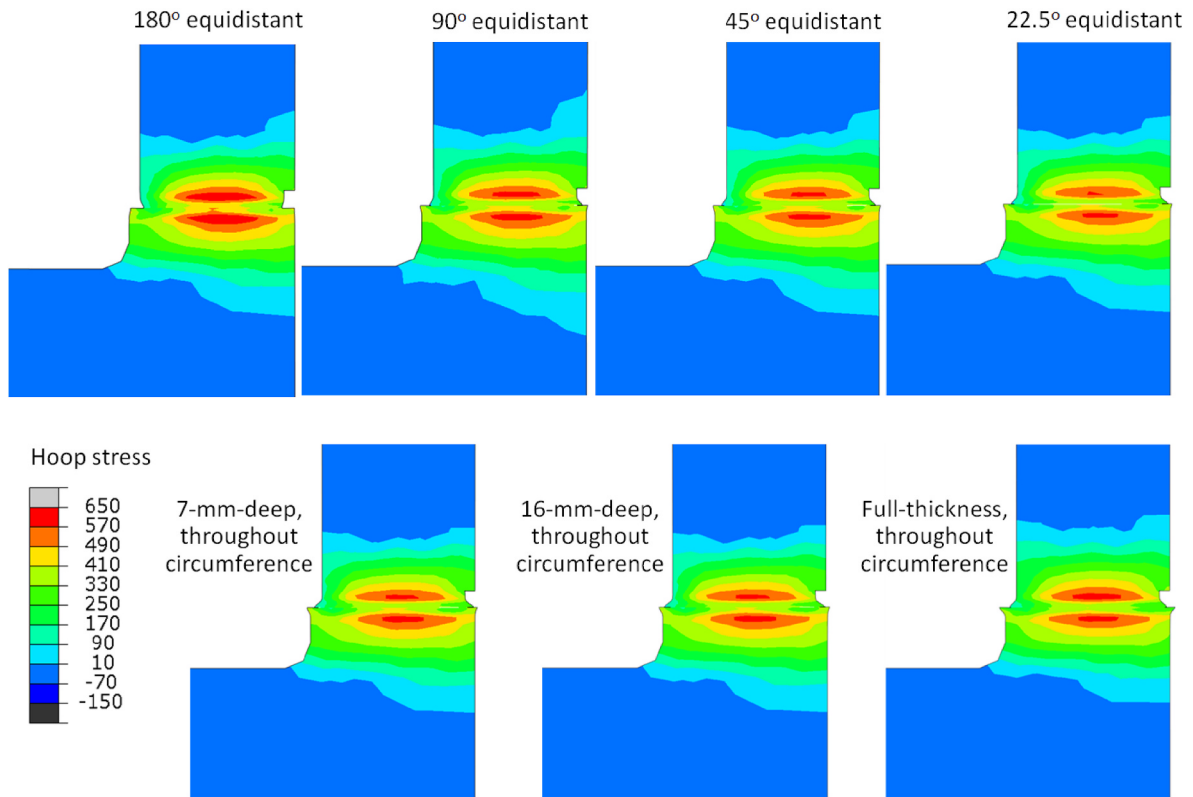

Fig. 21. Axial residual stress (unit: MPa) distributions on the axial section (steady-state welding region) with an angular distance of 180° from the EB weld start position for different restraint conditions.
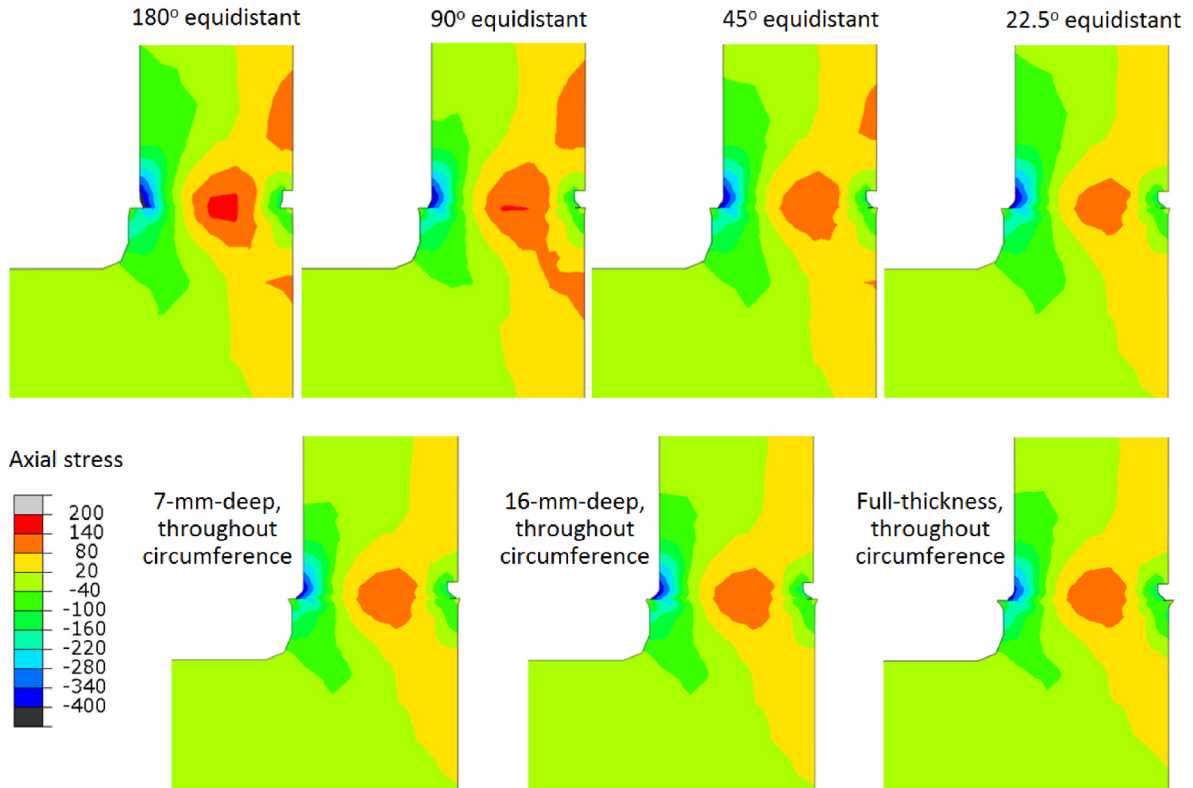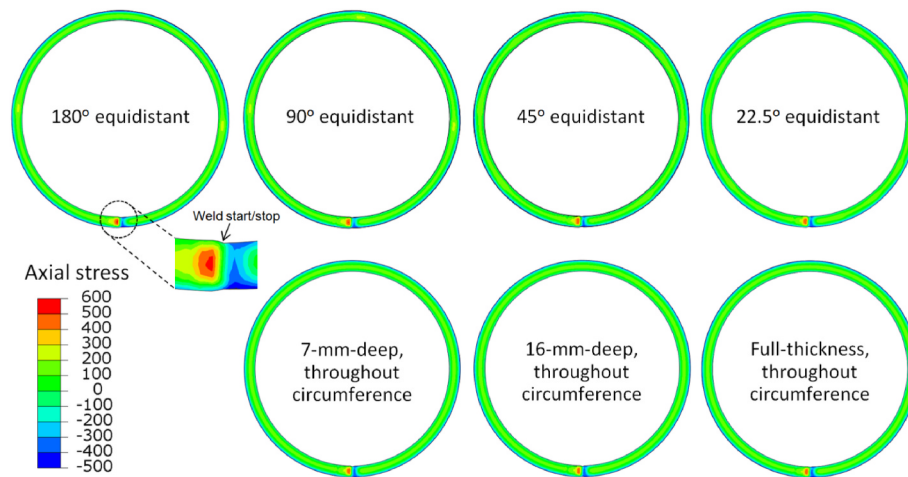
Fig. 22. Axial residual stress (unit: MPa) distributions on EB weld plane for different restraint conditions.
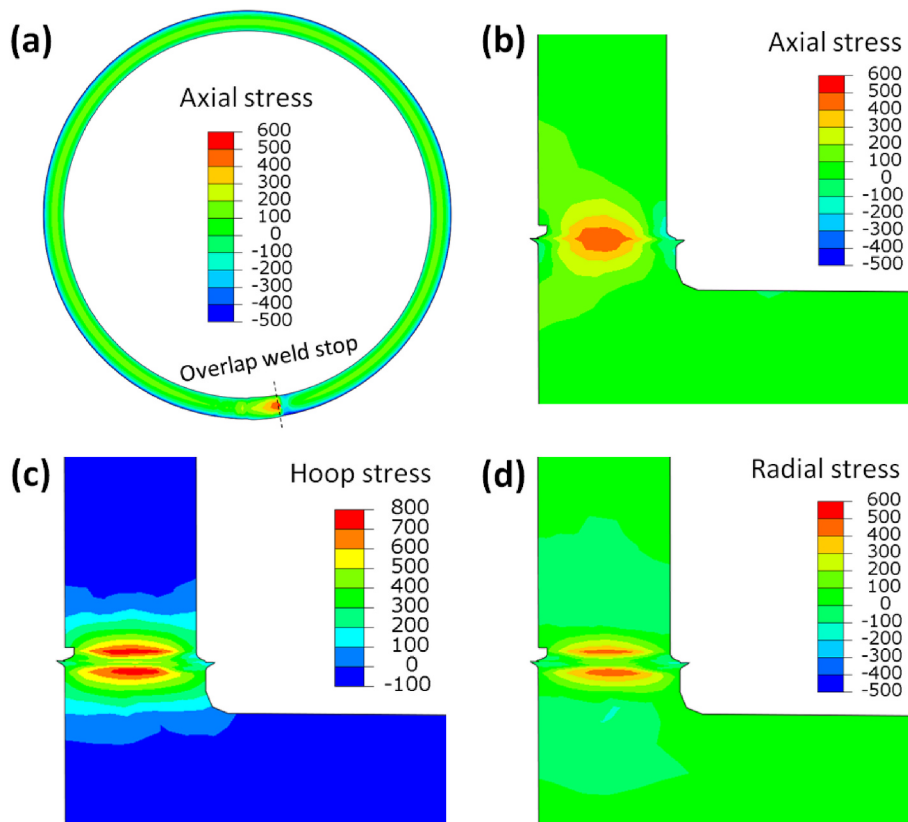

Fig. 23. Residual stress (unit: MPa) distributions after overlap EB welding: (a) axial stress on weld plane; (b), (c) and (d) show axial, hoop and radial stresses on the axial section where the stress magnitude is maximum.

circumferential EB weld are controlled by a similar mechanism to those observed at the stop positions of final capping beads or short repairs in conventional arc welds, but they are relatively much more severe, as a consequence of the EB welding process itself, which welds the entire thickness in a single pass, as well as the abrupt stop that has been modelled. The modelling approach adopted here means that the stop transient may be over-severe compared with a more gradual weld run-out, but the level of conservatism is as yet unknown.

A 150 mm long overlap of the EB welding was examined in the weld model to further investigate the stress concentration at the weld stop location. The results showed that a stress concentration similar to that without welding overlap developed around the overlap weld stop

location (Figs. 22 and 23). In other words, the stress concentration cannot be eliminated by changing the weld stop location. These modelling results demonstrated the challenge to handle the critical issues associated with EB weld stop, either with or without weld overlapping. Another important issue is the stress triaxiality near the weld stop location. Triaxial stresses of such a magnitude (Fig. 23) are a challenge to structural integrity. They could lead to cracking during welding if the microstructure in the final weld pool is unfavourable, due to chemical segregation or the formation of low toughness micro-constituents. Adequate post-weld heat treatment will also be important, and the degree of relaxation to be expected in the stop location is yet to be determined, given the high local triaxiality.
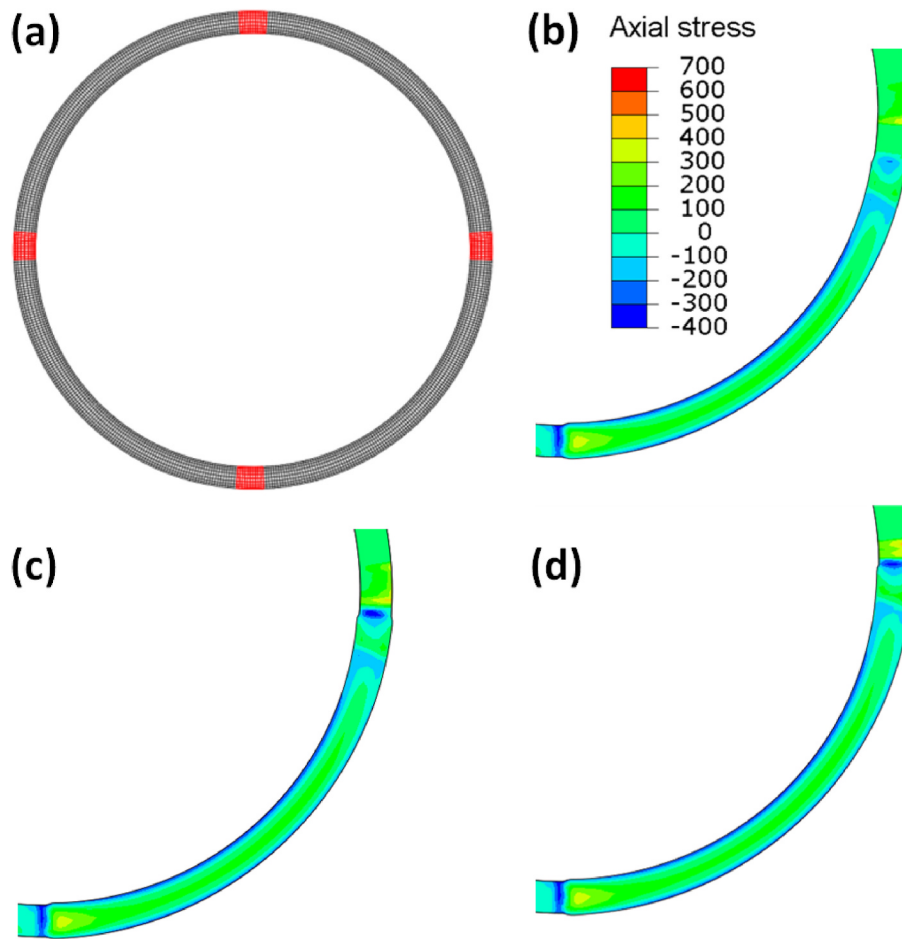
Fig. 24. (a) 90° equidistant tack welds which are 100 mm wide in circumferential direction; (b), (c) and (d) show the axial stress (unit: MPa) distributions on the EB weld plane when the shell-flange structure was welded over 81°, 85.5° and 90°, respectively.

Although the configuration of the tack welds has significant impact on the transient stress experienced by the tack welds during EB welding, its effect on the final residual stress in the welded shell-flange structure is insignificant (Figs. 19–22). A similar conclusion was also drawn for a SA508 Grade 4N steel EB weld plate [9]. During final cooling the EB weld had replaced the tack weld to provide the restraint that prevents separation of the two opposing components, and hence the tack welds do not make considerable difference to the final weld residual stress.

5. Concluding remarks

A 3D FE model was developed to simulate EB welding in a large SA508 low-alloy steel shell-flange structure, which is representative of actual engineering structures used in small modular reactors. The challenges overcome by the weld model include the complexity of both the prescribed restraint on the weld plane and the progressive development of self-restraint during EB welding, as well as the distinctive metallurgical behaviour in the narrow FZ/HAZ of the large structure. Circumferentially discrete tack welds with different intervals and widths, and circumferentially continuous tack welds with different depths, as well as overlap welding, were considered in the weld model. The following findings are summarised.

- An opening and sliding gap occurs due to the unique temperature field generated by the EB welding when no weld restraint is imposed, and the gap causes position mismatch between the opposing components during welding and an underfill defect in the final weld, demonstrating the necessity of weld restraint. Restraint through tack

welds effectively mitigates the gapping distortion, but it induces high transient tensile axial stress which could break the tack welds. For discrete tack welds, the restraint-induced peak tensile stress is insensitive to the change in the angular interval (or the number of tack welds), whereas it reduces with increasing the extent of each tack weld. For continuous tack welds, an increase in tack weld depth is helpful for reducing peak tensile stress. The continuous tack welds are preferred over the discrete tack welds, since the former can effectively reduce the tensile stress, thereby lowering the risk of tack weld breakage and loss of restraint during the EB welding.

- The different configurations of tack welds hardly affect the final residual stresses, since the tack welds have been replaced with the full penetration EB weld when the welding is completed, and the EB weld itself provides restraint from the potential separation of the two opposing components during cooling, which determines the final residual stress. The predicted radial and hoop residual stress distributions are typical for ferritic steel weldments subjected to SSPT, i.e., tensile stresses are suppressed in the FZ and HAZ, owing to the metallurgical expansion deformation during cooling, and the peak tensile stress is shifted towards the interface with the base material. The axial stress distribution is distinctive due to the difference in deformation and constraint in axial direction.

- A large concentration of residual stress is discovered in the weld stop region. High tensile stresses develop just behind the beam stop location and compressive stresses just ahead, with peak tensile stresses exceeding yield strength in the radial and axial directions, and approximately twice yield strength in the hoop direction. Overlap welding or change of weld stop location does not diminish

the stress concentration. This finding indicates that the weld stop location is most susceptible to cracking due to the high stress level. The abrupt weld stop transient assumed in the model is probably a factor in the stress magnitude predicted. Future work would be devoted to the simulation of a smooth run-out of welding to quantify the degree of conservatism.

CRediT authorship contribution statement

Yongle Sun: Conceptualization, Methodology, Software, Formal analysis, Investigation, Writing - Original Draft, Visualisation. **Mike Smith:** Conceptualization, Investigation, Funding acquisition, Writing - Review & Editing, Supervision, Project administration. **Thomas Dutilleul:** Investigation, Resources, Writing - Review & Editing. **Steve Jones:** Validation, Resources, Writing - Review & Editing.

Declaration of competing interest

The authors declare that they have no known competing financial interests or personal relationships that could have appeared to influence the work reported in this paper.

Data availability

Data underlying this study can be accessed through the Cranfield University repository at https://doi.org/10.17862/cranfield. rd.20407119.

Appendix

Table A1 summarises the temperature-dependent thermal and physical properties for the SA508 Grade 3 Class 1 steel considered in the EB weld model.

Table A1
Thermal and physical properties of SA508 Gr. 3 Cl.1 steel at different temperatures [36].

Temperature ($°C$)	Mean coefficient of thermal expansion (K^{-1})	Density ($g \cdot cm^{-3}$)	Specific heat ($J \cdot kg^{-1} \cdot K^{-1}$)	Thermal conductivity ($W \cdot m^{-1} \cdot K^{-1}$)	Young's modulus (GPa)	Poisson's ratio
20	–	7.81	442	39.5	199	0.294
100	1.25×10^{-5}	7.79	480	41.3	207	0.294
200	1.31×10^{-5}	7.76	531	42.5	209	0.294
300	1.36×10^{-5}	7.72	554	41.8	203	0.294
400	1.41×10^{-5}	7.69	605	39.6	189	0.294
500	1.44×10^{-5}	7.65	683	36.9	167	0.294
550	–	–	–	–	153	0.294
600	1.48×10^{-5}	7.61	750	34.7	137	0.294
650	–	–	–	–	119	0.294
700	1.50×10^{-5}	7.57	923	33.4	99	0.294
800	9.44×10^{-6}	7.64	839	33.2	–	–
900	1.10×10^{-5}	7.59	770	33.6	–	–
1000	1.23×10^{-5}	7.53	745	34.1	–	–
1100	1.33×10^{-5}	7.48	750	34.8	–	–
1200	1.41×10^{-5}	7.43	767	37.7	–	–
1400	–	–	–	–	10	0.294

For material plasticity, a nonlinear kinematic strain hardening model was adopted. The variation rate for each backstress component α_k is given below

$$\dot{\boldsymbol{\alpha}}_k = C_k \frac{1}{\sigma^0} (\boldsymbol{\sigma} - \boldsymbol{\alpha}) \dot{\bar{\varepsilon}}^{\mathrm{pl}} - \gamma_k \boldsymbol{\alpha}_k \dot{\bar{\varepsilon}}^{\mathrm{pl}} \tag{A1}$$

and the overall backstress is obtained by

$$\alpha = \sum_{k=1}^{N} \alpha_k \tag{A2}$$

where σ is the stress tensor, $\dot{\bar{\varepsilon}}^{\mathrm{pl}}$ is the equivalent plastic strain rate, σ^0 is the size of the yield surface, and C_k and γ_k are material parameters. The annealing temperature was taken to be 1300 °C. The temperature-dependent plastic properties for different microconstituents are given in Table A2.

Table A2
Material parameters adopted for the plasticity model at different temperatures.

	σ^0 (MPa)	C_1 (MPa)	γ_1	C_2 (MPa)	γ_2	Temperature (°C)
Base material	402	17400	346.84	4410	17.48	21
	340	19500	346.84	4510	17.48	100
	330	18200	346.84	4380	17.48	200
	320	28200	346.84	4210	17.48	300
	300	30600	346.84	3820	17.48	400
	260	38300	346.84	1460	17.48	500
	220	28000	346.84	0	17.48	550
	200	28000	346.84	0	17.48	600
	90	26000	346.84	0	17.48	650
	40	18000	346.84	0	17.48	700
	2	0	346.84	0	17.48	1300
Austenite	320	15000	75	0	17.48	21
	280	15000	75	0	17.48	200
	160	7500	75	0	17.48	600
	50	1875	75	0	17.48	800
	35	2250	75	0	17.48	900
	12	0	75	0	17.48	1100
	10	0	75	0	17.48	1300
Martensite	870	22151	100.5	3841.5	8.65	21
	730	23834	100.5	3979.4	8.65	300
	660	18590	100.5	3128	8.65	400
	160	13580	100.5	2797	8.65	500
	210	14350	100.5	2776	8.65	600
	25	0	100.5	0	8.65	1300
Bainite	420	23573	104.88	3903.2	8.77	25
	420	21649	104.88	3131.6	8.77	400
	306	13487	104.88	2863.4	8.77	600
	160	9967.2	104.88	1490.5	8.77	700
	25	0	104.88	0	8.77	1300
Ferrite/pearlite	420	23309	104.88	3909.9	8.77	25
	380	22837	104.88	4102.7	8.77	100
	360	27349	104.88	4585.5	8.77	200
	290	18353	104.88	3214.8	8.77	400
	180	39008	104.88	3555.9	8.77	500
	90	2517.1	104.88	3049.5	8.77	600
	25	0	104.88	0	8.77	1300

References

[1] M.S. Węglowski, S. Błacha, A. Phillips, Electron beam welding – techniques and trends – Review, Vacuum 130 (2016) 72–92.

[2] A. Sanderson, C. Punshon, J. Russell, Advanced welding processes for fusion reactor fabrication, Fusion Eng. Des. 49 (2000) 77–87.

[3] S. Shono, S. Kawaguchi, M. Sugino, N. Nakajima, Application of New Welding Technology for the Manufacturing of Nuclear Pressure Vessels, Design & Analysis, Elsevier1989, pp. 1279-1286.

[4] M.C. Smith, A.N. Vasileiou, D.W. Rathod, J. Francis, N.M. Irvine, Y. Sun, in: A Review of Welding Research within the New Nuclear Manufacturing (NNUMAN) Programme, Pressure Vessels and Piping Conference, American Society of Mechanical Engineers, 2017. V06BT06A072.

[5] A.N. Vasileiou, M.C. Smith, J.A. Francis, J. Balakrishnan, Y. Liang Wang, G. Obasi, M. Grace Burke, E.J. Pickering, D. Gandy, N.M. Irvine, Development of microstructure and residual stresses in electron beam welds in low alloy pressure vessel steels, Mater. Des. (2021), 109924.

[6] D. Rathod, J. Francis, A. Vasileiou, M. Roy, P. English, J. Balakrishnan, M. Smith, N. Irvine, Residual stresses in arc and electron-beam welds in 130 mm thick SA508 steel: Part 1-Manufacture, Int. J. Pres. Ves. Pip. 172 (2019) 313–328.

[7] A. Vasileiou, M. Smith, J. Francis, D. Rathod, J. Balakrishnan, N. Irvine, Residual stresses in arc and electron-beam welds in 130 mm thick SA508 steel: Part 2–measurements, Int. J. Pres. Ves. Pip. 172 (2019) 379–390.

[8] J. Balakrishnan, A. Vasileiou, J. Francis, M. Smith, M. Roy, M. Callaghan, N. Irvine, Residual stress distributions in arc, laser and electron-beam welds in 30 mm thick SA508 steel: a cross-process comparison, Int. J. Pres. Ves. Pip. 162 (2018) 59–70.

[9] Y.L. Sun, A.N. Vasileiou, E.J. Pickering, J. Collins, G. Obasi, V. Akrivos, M.C. Smith, Impact of weld restraint on the development of distortion and stress during the electron beam welding of a low-alloy steel subject to solid state phase transformation, Int. J. Mech. Sci. 196 (2021), 106244.

[10] M.C. Smith, Y. Sun, V. Akrivos, A. Vasileiou, E. Pickering, N. Irvine, A. Carruthers, J. Collins, Electron Beam Welding in SA508 Grade 4N and Grade 3 Class 1 Thick-Section Steels, Technical Report The University of Manchester, 2019.

[11] P. Withers, Residual stress and its role in failure, Rep. Prog. Phys. 70 (12) (2007) 2211.

[12] J.A. Francis, H.K.D.H. Bhadeshia, P.J. Withers, Welding residual stresses in ferritic power plant steels, Mater. Sci. Technol. 23 (9) (2007) 1009–1020.

[13] S. Bate, M. Smith, Determination of residual stresses in welded components by finite element analysis, Mater. Sci. Technol. 32 (14) (2016) 1505–1516.

[14] P. Bouchard, Code characterisation of weld residual stress levels and the problem of innate scatter, Int. J. Pres. Ves. Pip. 85 (3) (2008) 152–165.

[15] M. Kocak, I. Hadley, S. Szavai, Y. Tkach, N. Taylor, in: FITNET Fitness-For-Service (FFS) Annex vol. 2, GKSS Research Centre, Geesthacht, Germany, 2008.

[16] H. Dai, J. Francis, H. Stone, H. Bhadeshia, P. Withers, Characterizing phase transformations and their effects on ferritic weld residual stresses with X-rays and neutrons, Metall. Mater. Trans. 39 (13) (2008) 3070.

[17] B. Pellereau, C. Gill, P. Hurrell, E. Kingston, in: Residual Stress Modelling in a Thick-Sectioned Electron Beam Weld, Pressure Vessels and Piping Conference, American Society of Mechanical Engineers, 2013. V06BT06A085.

[18] B. Baufeld, T. Dutilleul, Electron beam welding of large components for the nuclear industry, in: MATEC Web of Conferences, EDP Sciences, 2019, 02009.

[19] C.P. Chea, Y. Bai, X. Pan, M. Arashpour, Y. Xie, An integrated review of automation and robotic technologies for structural prefabrication and construction, Transport. Saf. Environ. 2 (2) (2020) 81–96.

[20] P. Withers, M. Turski, L. Edwards, P. Bouchard, D. Buttle, Recent advances in residual stress measurement, Int. J. Pres. Ves. Pip. 85 (3) (2008) 118–127.

[21] M.V. Li, D.V. Niebuhr, L.L. Meekisho, D.G. Atteridge, A computational model for the prediction of steel hardenability, Metall. Mater. Trans. B 29 (3) (1998) 661–672.

[22] G. Obasi, E.J. Pickering, A.N. Vasileiou, Y.L. Sun, D. Rathod, M. Preuss, J.A. Francis, M.C. Smith, Measurement and prediction of phase transformation kinetics in a nuclear steel during rapid thermal cycles, Metall. Mater. Trans. 50 (4) (2019) 1715–1731.

[23] C.J. Hamelin, O. Muránsky, M.C. Smith, T.M. Holden, V. Luzin, P.J. Bendeich, L. Edwards, Validation of a numerical model used to predict phase distribution and residual stress in ferritic steel weldments, Acta Mater. 75 (2014) 1–19.

[24] A.N. Vasileiou, M.C. Smith, J. Balakrishnan, J.A. Francis, C.J. Hamelin, The impact of transformation plasticity on the electron beam welding of thick-section ferritic steel components, Nucl. Eng. Des. 323 (2017) 309–316.

[25] Y.L. Sun, G. Obasi, C.J. Hamelin, A.N. Vasileiou, T.F. Flint, J.A. Francis, M.C. Smith, Characterisation and modelling of tempering during multi-pass welding, J. Mater. Process. Technol. 270 (2019) 118–131.

[26] Y.L. Sun, G. Obasi, C.J. Hamelin, A.N. Vasileiou, T.F. Flint, J. Balakrishnan, M.C. Smith, J.A. Francis, Effects of dilution on alloy content and microstructure in multi-pass steel welds, J. Mater. Process. Technol. 265 (2019) 71–86.

[27] R. Smith, FEAT-WMT: Weld-modelling Tool User Guide, FeatPlus Limited, 2018.

[28] Y.L. Sun, C.J. Hamelin, T.F. Flint, A.N. Vasileiou, J.A. Francis, M.C. Smith, Prediction of dilution and its impact on the metallurgical and mechanical behavior of a multipass steel weldment, J. Pressure Vessel Technol. 141 (6) (2019).

[29] T.F. Flint, J.A. Francis, M.C. Smith, J. Balakrishnan, Extension of the double-ellipsoidal heat source model to narrow-groove and keyhole weld configurations, J. Mater. Process. Technol. 246 (2017) 123–135.

[30] J. Leblond, J. Devaux, A new kinetic model for anisothermal metallurgical transformations in steels including effect of austenite grain size, Acta Metall. 32 (1) (1984) 137–146.

[31] J. Kirkaldy, D. Venugopalan, Prediction of microstructure and hardenability in low alloy steels, in: Proceedings of the International Conference on Phase Transformation in Ferrous Alloys, 1983, AIME, 1983.

[32] D.P. Koistinen, R.E. Marburger, A general equation prescribing the extent of the austenite-martensite transformation in pure iron-carbon alloys and plain carbon steels, Acta Metall. 7 (1959) 59–60.

[33] J.A. Francis, M. Turski, P.J. Withers, Measured residual stress distributions for low and high heat input single weld beads deposited on to SA508 steel, Mater. Sci. Technol. 25 (3) (2009) 325–334.

[34] D. Smith, G. Zheng, P. Hurrell, C. Gill, B. Pellereau, K. Ayres, D. Goudar, E. Kingston, Measured and predicted residual stresses in thick section electron beam welded steels, Int. J. Pres. Ves. Pip. 120 (2014) 66–79.

[35] D. Deng, H. Murakawa, Prediction of welding residual stress in multi-pass butt-welded modified 9Cr–1Mo steel pipe considering phase transformation effects, Comput. Mater. Sci. 37 (3) (2006) 209–219.

[36] M.C. Smith, S. Bate, P.J. Bouchard, in: Simple Benchmark Problems for Finite Element Weld Residual Stress Simulation, Pressure Vessels and Piping Conference, American Society of Mechanical Engineers, 2013. V06BT06A087.

2022-08-30

Assessing and mitigating the distortion and stress during electron beam welding of a large shell-flange structure

Sun, Yongle

Elsevier